
Article:
Lai, W., Yu, T., Bui, T.Q. et al. (4 more authors) (2017) 3-D elasto-plastic large deformations: IGA simulation by Bézier extraction of NURBS. Advances in Engineering Software. ISSN 1873-5339

https://doi.org/10.1016/j.advengsoft.2017.02.011

Full Research Paper:

3-D elasto-plastic large deformations: IGA simulation by Bézier extraction of NURBS

Wenjiang Lai[a], Tiantang Yu[a,*], Tinh Quoc Bui[b,c,*], Zhiguo Wang[a,d],
Raj Das[e], Jose L. Curiel-Sosa[f], Sohichi Hirose[c]

[a] Department of Engineering Mechanics, Hohai University, Nanjing 211100, PR China.
[b]Institute for Research and Development, Duy Tan University, Da Nang City, Vietnam
[c]Department of Civil and Environmental Engineering, Tokyo Institute of Technology, 2-12-1-W8-22, Ookayama, Meguro-ku, Tokyo 152-8552, Japan.
[d]School of Management Science and Engineering, Anhui University of technology, Ma'anshan 243002, PR China.
[e]Department of Mechanical Engineering, Centre for Advanced Composite Materials, University of Auckland, New Zealand
[f]Department of Mechanical Engineering, The University of Sheffield, Sir Frederick Mappin Building, Mappin Street, S1 3JD Sheffield, United Kingdom

Abstract

This paper is devoted to numerical simulation of elasto-plastic large deformation in three-dimensional (3-D) solids using isogeometric analysis (IGA) based on Bézier extraction of NURBS (non-uniform rational B-splines), due to some inherently desirable features. The Bézier extraction operation decomposes the NURBS basis functions into a set of linear combination of Bernstein polynomials, and a set of C^0-continuity Bézier elements are thus obtained. The data structure is thus similar to traditional finite element method (FEM). Consequently, the IGA based on Bézier extraction of NURBS can be embedded in existing FEM codes, and more importantly, as have been shown in literature that higher accuracy over traditional FEM can be gained. The main features distinguish between the IGA and FEM are the exact geometry description with fewer control points, high-order continuity, high accuracy, especially the NURBS basis functions are capable of describing both geometry and solution fields where the FEM does not. The present kinematic is based on the Total Lagrange description due to the elasto-plastic large deformation with deformation history. The results for the distributions of displacements, von Mises stress, yielded zones, and force-displacement curves are computed and analyzed. For convenience in verification of numerical results, the same numerical examples have additionally been computed with the FEM using ABAQUS. It is found that most numerical results obtained by the developed IGA are acceptable and in good agreement with FEM solutions.

Keywords: 3-D; elasto-plastic large deformation; Isogeometric analysis; NURBS; Bézier extraction, FEM.

[*] Corresponding authors: Hohai University, PR China (T.T. Yu) & Duy Tan University, Da Nang City, Vietnam (T. Q. Bui).
Email addresses: tiantangyu@hhu.edu.cn (T.T. Yu); buiquoctinh@duytan.edu.vn; tinh.buiquoc@gmail.com (T.Q. Bui).

1. Introduction

The main problem addressed in this manuscript is the prediction of mechanical behaviors of three-dimensional (3-D) elasto-plastic solids under large deformations and statically applied load using an effective numerical approach. The elasto-plastic large deformation behavior is very common in the process of engineering design and analysis. In real engineering applications, large deformations of elasto-plastic materials are often encountered in, for instance, sheet metal forming or structural crashworthiness [1, 2]. The existence of material nonlinearity and geometric nonlinearity usually causes the modeling and simulations difficultly. The calculation accuracy is not always satisfactory, and still remains a challenging task. The accurate prediction of mechanical behaviors of elasto-plastic large deformation is absolutely indispensable for any steps of proper design of structural and mechanical components [3, 4]. Basically, the geometric nonlinearity is caused by the large displacement of the structural deformation. The strain term is a nonlinear matrix containing higher order trace, and the deformation process can not be described on the basis of the initial state. Consequently, the equilibrium position is unknown. In such circumstance, incremental methods have to be developed for solving nonlinear problems. In the last decades, the authors of several important and favorite textbooks in the field, for instance, see [5-7], who have made great contributions to the development and perfection of the geometric nonlinear theories.

In line of 3-D elastoplastic large deformation problems, Khoei and Lewis [2] described a general framework for finite element simulation of metal powder forming. Their approach is based on a total and updated Lagrangian formulation, an adaptive finite element strategy, and automatic remeshing techniques. Chiou et al. [4] developed a 3-D finite element code for large strain elastic-plastic solids. They used their own theory by decomposing the deformation gradient into a product of the elastic and plastic parts, instead of a combination of elastic and plastic strain rates. They stated that their solutions for elastic-plastic solids are path-dependent. The numerical results still may not be acceptable if the incremental step size is too large, even through the obtained solutions are stable. Reese et al [8] proposed a new locking-free brick element for 3-D large deformation problems in finite elasticity on the basis of enhanced strain method. Their new elements are free of locking, which is often caused by using isoparametric low-order elements in modeling elasto-plastic large deformation, arising mainly in bending-dominated situation and in the limit of incompressibility. Puso and Solberg [9] devoted a stabilized nodally integrated tetrahedral element, an effective low-order element that can circumvent the poor performance of classical linear tetrahedral element in problems with plasticity, nearly incompressible materials and acute bending. Areias and Matous [10] presented a 3-D mixed stabilized four-node tetrahedron with nonlocal pressure for hyperelastic materials of reinforced elastomers. Their element is unconditionally convergent and free of spurious pressure modes. Duster and Rank [11] applied the high-order finite element method to the problem of large plastic deformation, obtained high convergence rate and accurate solution, and there is no self-locking phenomenon. Recently, Pascon and Coda [3, 12-14], in contrast, developed high-order full integrated tetrahedral elements and successfully applied them to large deformation analysis of, for instance, elastoplastic homogeneous materials, elastic functionally graded materials, elastoplastic functionally graded materials, and functionally graded rubber-like materials. Nevertheless, there are a number of previous studies available in literature, and most of them are in 2-D and are carried out using the FEM [15, 16]. In the contrary to the low-order finite elements, the present study however is devoted to 3-D large deformation analysis of elasto-plastic materials, but using an effective, accurate, high order and locking-free isogeometric finite element method.

Isogeometric analysis (IGA) pioneered by Hughes et al. [17] owns many advantages as compared with the traditional FEM. The exact geometrical representation, high-order continuity, and high accuracy are those that substantially exhibit the implication of the IGA to be an effective numerical tool nowadays. The inherently desirable characteristics of IGA makes it superior to the classical FEM in many aspects and has successfully applied to many engineering problems including plate/shell structures [18-25], structural optimization [26], contact problem [27], fluid mechanics [28], fluid–structure interaction [29], damage and fracture mechanics [30-33], and unsaturated flow problem in porous media [34].

The IGA has also been applied to the modeling of material and geometric nonlinear problems such as elasto-plastic behavior, nearly incompressible behavior and large deformation behavior [35-38]. In Elguedj and Hughes [35], the IGA is applied to solve the nearly incompressible large strain plasticity problem, and it is found that the displacement and relative displacement of the specific position of the reaction force curve, often in the plastic problem is misleading metric. In their analysis, high-order NURBS cell does not appear low-order finite element mesh self-locking phenomenon, and can accurately describe the phenomenon of large plastic deformation, calculated accurate results. Basically, the implementation of the conventional IGA approach based on NURBS is often complex since their basis functions are not confined to one single element, but span over a global domain instead. Recently, the construction of the Bézier extraction operator of NURBS integrated into the IGA has been described, e.g., see [39, 40], by which the NURBS basis functions are thus decomposed into linear combinations of Bernstein polynomials. This development brings great benefit as it provides an element structure for IGA that can be incorporated into any existing FEM code. In other words, this transformation makes it possible to use C^0-continuous Bézier elements as the finite element representation in IGA, thus a local data structure for IGA is close to that for traditional FEM. The IGA implementation can now be made similarly to that of traditional FEM.

In addition, IGA data structures based on Bézier extraction of T-splines is also introduced recently in [41]. Based on Bézier extraction and spline reconstruction, a Bézier projection for local projection, refinement, and coarsening of NURBS and T-splines was proposed by Thomas et al [42], which results in an element-based formulation that may easily be implemented in existing finite element codes. Irzal et al [43] developed an interface element of the IGA through Bézier extraction, which can be casted in the same framework as the conventional interface element. Evans et al. [44] extended Bézier extraction to HASTS, which are utilized as a basis for adaptive IGA. Schillinger et al [45] and Rypl et al. [46] further put their efforts to some studies about the computational efficiency of numerical quadrature schemes in IGA based on Bézier extraction. However, most of the existing studies using the IGA based on Bézier extraction have been limited to two-dimensional (2-D) elastic problems only. In this manuscript, the IGA based on Bézier extraction of NURBS will be further extended to large deformation analysis of 3-D elasto-plastic solids under static loading condition. This interesting work, in fact, has not been carried out in literature so far. Indeed, this is a much more difficult and challenging task as compared to 2-D problems, due to the material and geometrical nonlinearities plus complicated inherent configuration of 3-D models. The accuracy and the performance of our present 3-D IGA method will be verified by comparing the computed numerical results with respect to reference results derived from other numerical methods, e.g., FEM (ABAQUS). The mesh convergence, distributions of displacements and stresses, the force versus displacement curves, and other relevant field variables pertaining to large elasto-plastic deformation analysis will be analyzed to confirm the effectiveness of the developed IGA.

One crucial issue related to the simulation of elasto-plastic large deformation problems, which must be stated here, is the mesh distortion. In terms of the classical FEM, as it has stated and discussed in [47] that the higher order Lagrange elements are notoriously sensitive to mesh distortion, which in general prevents their use in modeling large deformation problems. In the contrary, the recent investigation of the IGA robustness by Lipton et al [48] demonstrated that higher-order and higher-continuity functions are able to lessen the impact of the distortions in most cases. In words, the IGA elements with the high-order NURBS basis functions appear to be quite robust out, to at least p=4 [48], implying that the robustness of the IGA NURBS elements increase with order. Nonetheless, their studies [47, 48] shed light on the potential, robustness and capability of the IGA to many large deformation problems of industrial interest. Inspired by aforementioned works, our motivation is to further extend the capability of the IGA to large elasto-plastic deformation problems. However, we are particularly interested in simulation of 3-D problems, which is rarely available in literature, and the Bézier extraction of NURBS which owns some advantages over the NURBS is taken instead.

The rest of the manuscript is structured as follows. In Section 2, three-dimensional IGA formulation based on Bézier extraction is presented. Fundamental equations of elasto-plastic large deformation problems are then given in Section 3. Subsequently, solution of nonlinear equations is described in Section 4. Three numerical examples in 3-D large elasto-plastic deformation are considered, analyzed, and discussed in Section 5. Some conclusions drawn from the study are stated in Section 6.

2. Three-dimensional isogeometric analysis based on Bézier extraction of NURBS

For the sake of completeness, we briefly present in this section the three-dimensional IGA based on Bézier extraction of NURBS, which will be used for the large deformation analysis of elasto-plastic materials. Detail can be found in Ref. [39, 40].

2.1 The NURBS basis functions [17-25]

An arbitrary set of B-spline basis functions can be defined in a corresponding standard parameter space $\xi \in [0,1]$. The one-dimensional parameter space is called a knot vector. A knot vector is a set of non-decreasing numbers in the parametric space as the following description

$$\mathbf{k}(\xi) = \left\{\xi_1, \xi_2, ..., \xi_{n+p+1}\right\}^T \tag{1}$$

where ξ_i is the i[th] knot with $\xi_i \le \xi_{i+1}$, the indices n and p denote, respectively, the number of basis functions and the order of B-spline basis function. According to the Cox-de Boor recursion formula, and for a given knot vector $\mathbf{k}(\xi)$, the B-spline basis function $N_{i,p}(\xi)$ is expressed as

$$N_{i,0}(\xi) = \begin{cases} 1 & \xi_i \le \xi < \xi_{i+1} \\ 0 & \text{otherwise} \end{cases} \qquad \text{for} \quad p=0 \tag{2}$$

and

$$N_{i,p}(\xi) = \frac{\xi - \xi_i}{\xi_{i+p} - \xi_i} N_{i,p-1}(\xi) + \frac{\xi_{i+p+1} - \xi}{\xi_{i+p+1} - \xi_{i+1}} N_{i+1,p-1}(\xi) \quad \text{for} \quad p \ge 1 \tag{3}$$

For modeling 3-D problems, the NURBS basis functions can be obtained directly from the tensor-product of three one-dimensional B-spline basis functions [49]

$$R^{p,q,r}_{i,j,k}(\xi,\eta,\zeta)=\frac{N_{i,p}(\xi)N_{j,q}(\eta)N_{k,r}(\zeta)w_{i,j,k}}{\sum_{\hat{i}=1}^{n}\sum_{\hat{j}=1}^{m}\sum_{\hat{k}=1}^{l}N_{\hat{i},p}(\xi)N_{\hat{j},q}(\eta)N_{\hat{k},r}(\zeta)w_{\hat{i},\hat{j},\hat{k}}}=\frac{N_{i,p}(\xi)N_{j,q}(\eta)N_{k,r}(\zeta)w_{i,j,k}}{W(\xi,\eta,\zeta)} \quad (4)$$

in which $N_{i,p}(\xi)$, $N_{j,q}(\eta)$ and $N_{k,r}(\zeta)$ are the B-spline basis functions of orders p, q, and r in the ξ, η and ζ directions, respectively; $N_{j,q}(\eta)$ and $N_{k,r}(\zeta)$ follow the recursive formula shown in Eqs. (2) and (3) with knot vector $\mathbf{k}(\eta)$ and $\mathbf{k}(\zeta)$, and the definition of $\mathbf{k}(\eta)$ and $\mathbf{k}(\zeta)$ is similar to that of $\mathbf{k}(\xi)$; $w_{i,j,k}$ are the weight, and $W(\xi,\eta,\varsigma)$ represent the weight function.

By defining $\mathbf{W}$ as the diagonal matrix of weights,

$$\mathbf{W}=\begin{bmatrix} w_1 & & & \\ & w_2 & & \\ & & O & \\ & & & w_n \end{bmatrix} \quad (5)$$

and let $\mathbf{N}(\xi,\eta,\varsigma)$ be the vector of B-spline basis functions, then Eq.(4) can be rewritten in matrix form

$$\mathbf{R}(\xi,\eta,\varsigma)=\frac{1}{W(\xi,\eta,\varsigma)}\mathbf{WN}(\xi,\eta,\varsigma) \quad (6)$$

Fig. 1 schematically illustrates the representation of a quadratic B-spline defined by the knot vectors $\Xi=\{0,0,0,1,2,2,2\}$, $H=\{0,0,0,1,2,3,3,3\}$ and $Z=\{0,0,0,1,1,1\}$. That is accomplished by assumption that, if two elements, three elements and one element are taken for the ξ, η and ζ directions, respectively. One can see from the figure that a B-spline basis function spans the parameter space composed of several elements. As a result, the NURBS function hence spans the parameter space also composed of several elements. Importantly, it can now easily be seen that implementing the NURBS basis function is arduous.

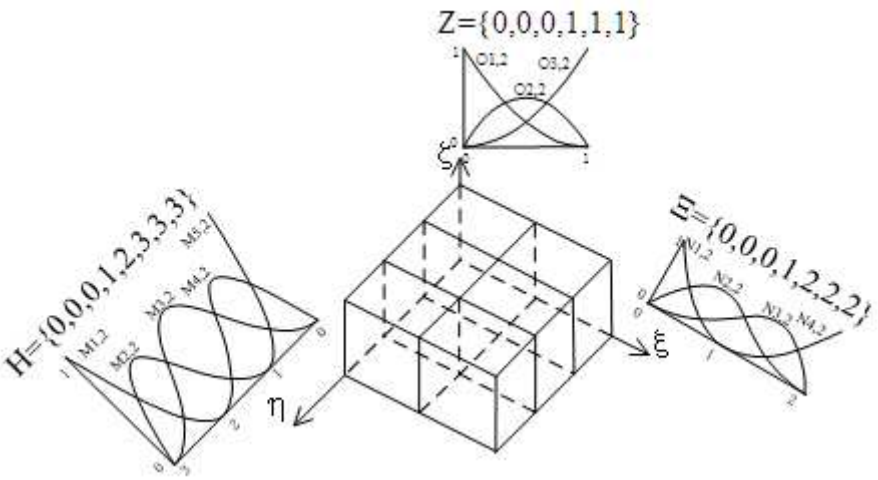

Fig. 1 Schematic representation of quadratic B-spline basis functions.

2.2 Bézier extraction of NURBS

Due to the complicated calculation of the NURBS basis functions as addressed in the previous section, the underlying idea behind the Bézier extraction of the NURBS is, as pointed out in [39], to provide an element structure for IGA that can be incorporated into any existing FEM code.

Basically, the Bézier extraction operation is to decompose the NURBS basis function into a set of linear combinations of Bernstein polynomials, and to obtain a set of C^0-continuity Bézier elements, which is similar to the Lagrange elements, once again, straightforwardly integrating into the existing FEM code. The Bézier decomposition is the consequence of the decomposing process of the NURBS basis functions into corresponding Bézier elements. The Bézier decomposition is attained by repeating all interior knots of a knot vector until they have a multiplicity equal to p. The degree of interior knots should be p +1 to produce the truly separate Bézier elements. However, the multiplicity equal to p is sufficient to represent the Bernstein polynomial that is the Bézier basis function.

Let $\mathbf{k}\left(\xi\right)=\left\{\xi_1,\xi_2,...,\xi_{n+p+1}\right\}^{\mathrm{T}}$ be the original knot vector, let us insert a new knot $\bar{\xi}\in[\xi_k,\xi_{k+1})$ ($k>p$) into the knot vector, the number of the new basis functions reaches $m=n+1$, and the new control points $\bar{P}_i$ can be deduced with old control points P_i [39, 40]

$$\bar{P}_i=\begin{cases}P_1 & i=1\\ \alpha_i P_i+\left(1-\alpha_i\right)P_{i-1} & 1<i<m\\ P_n & i=m\end{cases} \tag{7}$$

with

$$\alpha_i=\begin{cases}1 & i\le k-p\\ \dfrac{\bar{\xi}-\xi_i}{\xi_{i+p}-\xi_i} & k-p+1\le i\le k\\ 0 & i\ge k+1\end{cases} \tag{8}$$

It is worth noting that the knot values may be inserted multiple times, but it makes the continuity of the basis to be reduced by one for each repetition of a given knot value. The continuity of the curve, however, is preserved, provided that the control variables in Eqs.(7) and (8) are chosen.

According to [39, 40], the Bézier extraction operator of the j^{th} knot inserted is defined by

$$\mathbf{C}^j=\begin{bmatrix}\alpha_1 & 1-\alpha_2 & 0 & \mathrm{L} & & 0\\ 0 & \alpha_2 & 1-\alpha_3 & 0 & \mathrm{L} & 0\\ \mathrm{M} & & & \mathrm{O} & & \mathrm{M}\\ 0 & \mathrm{L} & & & \alpha_{n+j-1} & 1-\alpha_{n+j}\end{bmatrix} \tag{9}$$

$\mathbf{P}$ is the original control points, and let $\bar{\mathbf{P}}_1 = \mathbf{P}$, Eq. (7) can then be rewritten in matrix form

$$\bar{\mathbf{P}}_{j+1} = (\mathbf{C}^j)^T \bar{\mathbf{P}}_j \tag{10}$$

By defining $\{\bar{\xi}_1, \bar{\xi}_2, \mathrm{L}\ , \bar{\xi}_j, \mathrm{L}\ , \bar{\xi}_m\}$ is the set of inserted knots vector, the whole Bézier extraction operator yields

$$\mathbf{C}^T = (\mathbf{C}_m)^T (\mathbf{C}_{m-1})^T ... (\mathbf{C}_1)^T \tag{11}$$

Consequently, the relation between the new control points $\mathbf{P}^b$ after Bézier extraction and the original control points $\mathbf{P}$ can be expressed as

$$\mathbf{P}^b = \mathbf{C}^T \mathbf{P} \tag{12}$$

It is important to stress out here that inserting a new knot to the curve does not change the geometric shapes, and B-spline curves can now be defined by $\mathbf{C}(\xi) = \mathbf{P}^T \mathbf{N}(\xi)$, yielding the following relation

$$\mathbf{C}(\xi) = \left(\mathbf{P}^b\right)^T \mathbf{B}(\xi) = \left(\mathbf{C}^T \mathbf{P}\right)^T \mathbf{B}(\xi) = \mathbf{P}^T \mathbf{C}\mathbf{B}(\xi) = \mathbf{P}^T \mathbf{N}(\xi) \tag{13}$$

The relationship between the B-spline basis functions and Bernstein polynomials is thus obtained as

$$\mathbf{N}(\xi) = \mathbf{C}\mathbf{B}(\xi) \tag{14}$$

Using the same technique, we can infer the local 3-D Bézier extraction operator

$$\mathbf{C}^e = \mathbf{C}_\varsigma^k \otimes \mathbf{C}_\eta^j \otimes \mathbf{C}_\xi^i \tag{15}$$

in which $\mathbf{C}_\xi^i$, $\mathbf{C}_\eta^j$ and $\mathbf{C}_\varsigma^k$ respectively are the i^{th}, j^{th} and k^{th} univariate element Bézier extraction operator in the ξ, η and ζ directions, and e denotes the number of element. Through Eqs. (14) and (15), the local 3D relationship between the B-spline basis functions and Bernstein polynomials reaches:

$$\mathbf{N}^e(\xi, \eta, \varsigma) = \mathbf{C}^e \mathbf{B}^e(\xi, \eta, \varsigma) \tag{16}$$

In analysis, it is unnecessary to establish the global extraction operator. Instead, only establishment of the local extraction operator of each element is needed. The NURBS basis functions after Bézier extraction operator is now defined as

$$\mathbf{R}^e(\xi, \eta, \varsigma) = \frac{\mathbf{W}^e \mathbf{C}^e \mathbf{B}^e(\xi, \eta, \varsigma)}{\mathrm{W}^b(\xi, \eta, \varsigma)} \tag{17}$$

where $\mathbf{W}^e$ is the local NURBS weights, and $\mathrm{W}^b(\xi, \eta, \varsigma)$ finally yields the form

$$\mathrm{W}^b(\xi, \eta, \varsigma) = \sum_{i=1}^{(p+1)^{d_p}} \sum_{j=1}^{(q+1)^{d_p}} \sum_{k=1}^{(r+1)^{d_p}} \mathrm{B}_{i,p}(\xi)\, \mathrm{B}_{j,q}(\eta)\, \mathrm{B}_{k,r}(\varsigma)\, \mathrm{w}_{i,j,k}^b \tag{18}$$

with d_p representing the parameter dimensions.

The relationship between Bézier control points $\mathbf{P}^{b,e}$ and NURBS control points $\mathbf{P}^e$ can be written as

$$\mathbf{P}^{b,e} = \left(\mathbf{W}^{b,e}\right)^{-1} (\mathbf{C}^e)^T \mathbf{W}^e \mathbf{P}^e \tag{19}$$

with $\mathbf{W}^{b,e}$ defining the local Bézier weights, which is in diagonal matrix.

For 3-D model, the NURBS basis functions and control points, in matrix form, is expressed as

$$\mathbf{C}(\xi, \eta, \varsigma) = \mathbf{P}^T \mathbf{R}(\xi, \eta, \varsigma) \tag{20}$$

The NURBS 3-D model in C^0 continuous Bézier elements, by combining Eqs. (17), (19) and (20), can now be defined as

$$\mathbf{C}(\xi, \eta, \varsigma) = \frac{\left(\mathbf{W}^b \mathbf{P}^b\right)^T \mathbf{B}(\xi, \eta, \varsigma)}{\mathrm{W}^b(\xi, \eta, \varsigma)} \tag{21}$$

Additionally, Fig. 2 sketches the Bézier basis functions derived from B-spline basis functions as shown in Fig.1 by taking the Bézier extraction operator. The resulting basis function has been decomposed into a set of C^0 continuous Bézier elements with each element corresponding to a knot spans in the original knot vector.

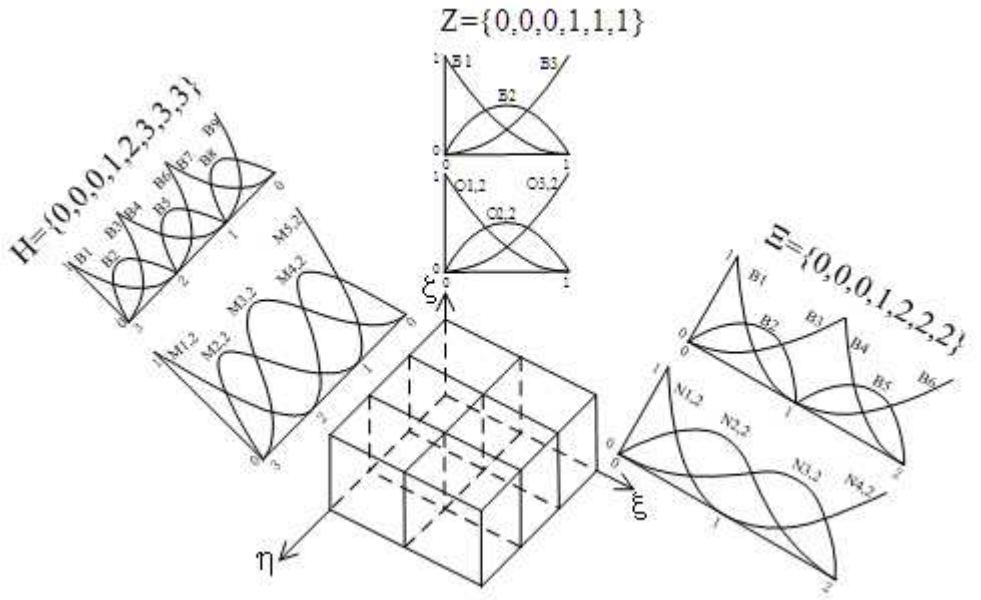

Fig. 2 Schematic representation of Bézier basis functions obtained from B-spline basis functions using the Bézier extraction operator.

3. Fundamental equations of elasto-plastic large deformations

In this section, we briefly present fundamental equations for elasto-plastic large deformation analysis of solids. Basically, the non-linearity in the elasto-plastic large deformation analysis is composed of two parts: the material nonlinearity and geometric nonlinearity. The basic description of elastoplastic constitutive models at finite strains is clear and detail can be found in Simo [15, 16] and Simo and Hughes [50]. Due to the elasto-plastic large deformation relating with the deformation history, the Total Lagrange description are used in this analysis. In that circumstance, meaning that, the initial state is the reference system, and the reference system is unchanged during the increment process.

In large deformation problem, the strain is expressed by the Green strain:

$$E_{ij} = \frac{1}{2}\left(\frac{\partial u_j}{\partial X_i} + \frac{\partial u_i}{\partial X_j} + \frac{\partial u_k}{\partial X_i}\frac{\partial u_k}{\partial X_j} \right) \tag{22a}$$

$$\bar{E}_{ij} = \frac{1}{2}\left(\frac{\partial \bar{u}_j}{\partial X_i} + \frac{\partial \bar{u}_i}{\partial X_j} + \frac{\partial \bar{u}_k}{\partial X_i}\frac{\partial \bar{u}_k}{\partial X_j} \right) \tag{22b}$$

The Green strain $\bar{E}_{ij}$ at time $t_{m+1} = t + Vt$ can be expressed as the sum of the Green strain E_{ij} at time $t_m = t$ and strain increment VE_{ij} in this time step Vt:

$$\bar{E}_{ij} = E_{ij} + VE_{ij} = \frac{1}{2}\left(\frac{\partial\left(u_j + Vu_j\right)}{\partial X_i} + \frac{\partial\left(u_i + Vu_i\right)_i}{\partial X_j} + \frac{\partial\left(u_k + Vu_k\right)}{\partial X_i}\frac{\partial\left(u_k + Vu_k\right)}{\partial X_j} \right) \tag{23}$$

It is trivial to obtain the strain increment VE_{ij} from the Eqs. (22) and (23):

$$\Delta E_{ij} = \Delta E_{ij0}^{L} + \Delta E_{ij1}^{L} + \Delta E_{ij}^{N} \tag{24}$$

with

$$VE_{ij0}^{L} = \frac{1}{2}\left(\frac{\partial Vu_j}{\partial X_i} + \frac{\partial Vu_i}{\partial X_j} \right) \tag{25a}$$

$$VE_{ij1}^{L} = \frac{1}{2}\left(\frac{\partial u_k}{\partial X_i}\frac{\partial Vu_k}{\partial X_j} + \frac{\partial Vu_k}{\partial X_i}\frac{\partial u_k}{\partial X_j} \right) \tag{25b}$$

$$VE_{ij}^{N} = \frac{1}{2}\left(\frac{\partial Vu_k}{\partial X_i}\frac{\partial Vu_k}{\partial X_j} \right) \tag{25c}$$

And Eq. (24) can be written in matrix form as

$$\Delta \mathbf{E} = \Delta \mathbf{E}_{L0} + \Delta \mathbf{E}_{L1} + \Delta \mathbf{E}_{N} \tag{26}$$

where

$$V\mathbf{E}_{L0} = \mathbf{L}V\mathbf{u} \tag{27a}$$

$$V\mathbf{E}_{L1} = \mathbf{AH}V\mathbf{u} \tag{27b}$$

$$V\mathbf{E}_{N} = \frac{1}{2}V\mathbf{AH}V\mathbf{u} \tag{27c}$$

with

$$\mathbf{L} = \begin{bmatrix} \frac{\partial}{\partial X_1} & 0 & 0 & \frac{\partial}{\partial X_2} & 0 & \frac{\partial}{\partial X_3} \\ 0 & \frac{\partial}{\partial X_2} & 0 & \frac{\partial}{\partial X_1} & \frac{\partial}{\partial X_3} & 0 \\ 0 & 0 & \frac{\partial}{\partial X_3} & 0 & \frac{\partial}{\partial X_2} & \frac{\partial}{\partial X_1} \end{bmatrix}^{T} \tag{28a}$$

$$\mathbf{A} = \begin{bmatrix} \frac{\partial \mathbf{u}^T}{\partial X_1} & 0 & 0 & \frac{\partial \mathbf{u}^T}{\partial X_2} & 0 & \frac{\partial \mathbf{u}^T}{\partial X_3} \\ 0 & \frac{\partial \mathbf{u}^T}{\partial X_2} & 0 & \frac{\partial \mathbf{u}^T}{\partial X_1} & \frac{\partial \mathbf{u}^T}{\partial X_3} & 0 \\ 0 & 0 & \frac{\partial \mathbf{u}^T}{\partial X_3} & 0 & \frac{\partial \mathbf{u}^T}{\partial X_2} & \frac{\partial \mathbf{u}^T}{\partial X_1} \end{bmatrix}^{T} \tag{28b}$$

$$\mathrm{V}\mathbf{A}=\begin{bmatrix} \dfrac{\partial \mathrm{V}\mathbf{u}^{\mathrm{T}}}{\partial \mathrm{X}_1} & 0 & 0 & \dfrac{\partial \mathrm{V}\mathbf{u}^{\mathrm{T}}}{\partial \mathrm{X}_2} & 0 & \dfrac{\partial \mathrm{V}\mathbf{u}^{\mathrm{T}}}{\partial \mathrm{X}_3} \\ 0 & \dfrac{\partial \mathrm{V}\mathbf{u}^{\mathrm{T}}}{\partial \mathrm{X}_2} & 0 & \dfrac{\partial \mathrm{V}\mathbf{u}^{\mathrm{T}}}{\partial \mathrm{X}_1} & \dfrac{\partial \mathrm{V}\mathbf{u}^{\mathrm{T}}}{\partial \mathrm{X}_3} & 0 \\ 0 & 0 & \dfrac{\partial \mathrm{V}\mathbf{u}^{\mathrm{T}}}{\partial \mathrm{X}_3} & 0 & \dfrac{\partial \mathrm{V}\mathbf{u}^{\mathrm{T}}}{\partial \mathrm{X}_2} & \dfrac{\partial \mathrm{V}\mathbf{u}^{\mathrm{T}}}{\partial \mathrm{X}_1} \end{bmatrix}^{\mathrm{T}} \tag{28c}$$

$$\mathbf{H}=\begin{Bmatrix} \mathbf{I}\dfrac{\partial}{\partial \mathrm{X}_1} \\ \mathbf{I}\dfrac{\partial}{\partial \mathrm{X}_2} \\ \mathbf{I}\dfrac{\partial}{\partial \mathrm{X}_3} \end{Bmatrix} \tag{28d}$$

Because of the displacement field is $\mathbf{u}=\mathbf{N}\mathbf{u}^{\mathrm{e}}$, Eq. (26) can be written as

$$\mathrm{V}\mathbf{E}=\bar{\mathbf{B}}\mathrm{V}\mathbf{u}^{\mathrm{e}} \tag{29a}$$

$$\delta\left(\mathrm{V}\mathbf{E}\right)=\mathbf{B}\delta\left(\mathrm{V}\mathbf{u}^{\mathrm{e}}\right) \tag{29b}$$

where

$$\bar{\mathbf{B}}=\mathbf{B}_{\mathrm{L0}}+\mathbf{B}_{\mathrm{L1}}+\bar{\mathbf{B}}_{\mathrm{N}}=\mathbf{B}_{\mathrm{L0}}+\mathbf{B}_{\mathrm{L1}}+\mathrm{V}\mathbf{A}\mathbf{H}\mathbf{N} \tag{30a}$$

$$\mathbf{B}=\mathbf{B}_{\mathrm{L0}}+\mathbf{B}_{\mathrm{L1}}+\mathbf{B}_{\mathrm{N}}=\mathbf{B}_{\mathrm{L0}}+\mathbf{B}_{\mathrm{L1}}+\mathbf{A}\mathbf{H}\mathbf{N} \tag{30b}$$

Here $\mathbf{B}_{\mathrm{L0}}=\mathbf{L}\mathbf{N}$ and $\mathbf{B}_{\mathrm{L1}}=\mathbf{A}\mathbf{H}\mathbf{N}$ have no connection with $\mathrm{V}\mathbf{u}^{\mathrm{e}}$, and $\mathbf{B}_{\mathrm{L0}}$ equivalents to the strain matrix $\mathbf{B}$ in small deformation problems, $\mathbf{B}_{\mathrm{L1}}$ represents the displacement effect of the linear incremental strain $\mathrm{V}\mathbf{E}_{\mathrm{L}}$.

The balance equation at time $\mathrm{t}_{\mathrm{m+1}}=\mathrm{t}+\mathrm{V}\mathrm{t}$ can be obtained according to the energy-variational principle:

$$\int_{\mathrm{V}_0}\delta\bar{\mathbf{E}}\bar{\mathbf{S}}\mathrm{d}\mathrm{V}=\int_{\mathrm{V}_0}\delta\bar{\mathbf{u}}^{\mathrm{T}}\mathbf{p}_0\mathrm{d}\mathrm{V}+\int_{\mathrm{A}_0}\delta\bar{\mathbf{u}}^{\mathrm{T}}\mathbf{q}_0\mathrm{d}\mathrm{A} \tag{31}$$

Because of the displacement $\mathbf{u}$ and strain $\mathbf{E}$ are known at time $\mathrm{t}_{\mathrm{m}}=\mathrm{t}$, it is possible to obtain the following formula:

$$\delta\left(\bar{\mathbf{u}}\right)=\delta\left(\mathrm{V}\mathbf{u}\right)=\mathbf{N}\delta\left(\mathrm{V}\mathbf{u}^{\mathrm{e}}\right) \tag{32a}$$

$$\delta\left(\bar{\mathbf{E}}\right)=\delta\left(\mathrm{V}\bar{\mathbf{E}}\right)=\mathbf{B}\delta\left(\mathrm{V}\mathbf{u}^{\mathrm{e}}\right) \tag{32b}$$

By substituting Eq. (7) into Eq. (6), and considering $\delta\left(\mathrm{V}\mathbf{u}^{\mathrm{e}}\right)$ is arbitrary, one can get:

$$\int_{V_0}\mathbf{B}^{\mathrm{T}}\bar{\mathbf{S}}\mathrm{dV}=\int_{V_0}\mathbf{N}^{\mathrm{T}}\mathbf{p}_0\mathrm{dV}+\int_{A_0}\mathbf{N}^{\mathrm{T}}\mathbf{q}_0\mathrm{dA} \tag{33}$$

The above formula can be written in the form of incremental:

$$\psi\left(\mathrm{V}\mathbf{u}^{\mathrm{e}}\right)=\int_{V_0}\mathbf{B}^{\mathrm{T}}\mathrm{V}\mathbf{S}\mathrm{dV}+\int_{V_0}\mathbf{B}_{\mathrm{N}}^{\mathrm{T}}\mathbf{S}\mathrm{dV}+\int_{V_0}\left(\mathbf{B}_{\mathrm{L0}}^{\mathrm{T}}+\mathbf{B}_{\mathrm{L1}}^{\mathrm{T}}\right)\mathbf{S}\mathrm{dV}-\bar{\mathbf{F}}_0=0 \tag{34}$$

where $\bar{\mathbf{F}}_0=\int_{V_0}\mathbf{N}^{\mathrm{T}}\mathbf{p}_0\mathrm{dV}+\int_{A_0}\mathbf{N}^{\mathrm{T}}\mathbf{q}_0\mathrm{dA}$

From Eq. (34), the following equations can be obtained by using two-step linearization approximation.

First, strain-displacement transformation matrix linearization is achieved by substituting $\mathbf{B}_{\mathrm{L0}}+\mathbf{B}_{\mathrm{L1}}$ for $\mathbf{B}$:

$$\mathrm{V}\mathbf{E}=\mathbf{B}\mathrm{V}\mathbf{u}\ \text{ turn into }\ \mathrm{V}\mathbf{E}\approx\left(\mathbf{B}_{\mathrm{L0}}+\mathbf{B}_{\mathrm{L1}}\right)\mathrm{V}\mathbf{u} \tag{35}$$

Second, strain increment and stress increment are expressed by linearization: $\mathrm{d}\mathbf{S}=\mathbf{D}_{\mathrm{T}}\mathrm{d}\mathbf{E}$ turn into $\Delta\mathbf{S}=\int_{\mathrm{E}}^{\mathrm{E}+\Delta\mathrm{E}}\mathbf{D}_{\mathrm{T}}\mathrm{d}\mathbf{E}$, where $\mathbf{D}_{\mathrm{T}}$ is the elasto-plastic matrix at time $\mathrm{t}_{\mathrm{m}}=\mathrm{t}$.

$$\int_{V_0}\mathbf{B}^{\mathrm{T}}\mathrm{V}\mathbf{S}\mathrm{dV}=\int_{V_0}\mathbf{B}^{\mathrm{T}}\mathbf{D}\mathrm{V}\mathbf{E}\mathrm{dV}\approx\left(\int_{V_0}\left(\mathbf{B}_{\mathrm{L0}}^{\mathrm{T}}+\mathbf{B}_{\mathrm{L1}}^{\mathrm{T}}\right)\mathbf{D}_{\mathrm{T}}\left(\mathbf{B}_{\mathrm{L0}}+\mathbf{B}_{\mathrm{L1}}\right)\mathrm{dV}_0\right)\mathrm{V}\mathbf{u}^{\mathrm{e}}=\mathbf{K}_{\mathrm{L}}\mathrm{V}\mathbf{u} \tag{36}$$

$$\int_{V_0}\mathbf{B}_{\mathrm{N}}^{\mathrm{T}}\mathbf{S}\mathrm{dV}=\left(\int_{V_0}\mathbf{G}^{\mathrm{T}}\mathbf{M}\mathbf{G}\mathrm{dV}_0\right)\mathrm{V}\mathbf{u}^{\mathrm{e}}=\left(\int_{V_0}\bar{\mathbf{G}}^{\mathrm{T}}\bar{\mathbf{M}}\bar{\mathbf{G}}\mathrm{dV}_0\right)\mathrm{V}\mathbf{u}^{\mathrm{e}}=\mathbf{K}_{\mathrm{s}}\mathrm{V}\mathbf{u} \tag{37}$$

$$\int_{V_0}\left(\mathbf{B}_{\mathrm{L0}}^{\mathrm{T}}+\mathbf{B}_{\mathrm{L1}}^{\mathrm{T}}\right)\mathbf{S}\mathrm{dV}=\mathbf{F}_{\mathrm{s}} \tag{38}$$

where $\mathbf{K}_{\mathrm{L}}$ is the stiffness matrix of linear strain, $\mathbf{K}_{\mathrm{s}}$ is the stiffness matrix of nonlinear strain, and $\mathbf{F}_{\mathrm{s}}$ is the equivalent nodal force vector at time $\mathrm{t}_{\mathrm{m}}=\mathrm{t}$.

One can finally get linearized balance equation:

$$\left(\mathbf{K}_{\mathrm{s}}+\mathbf{K}_{\mathrm{L}}\right)\mathrm{V}\mathbf{u}=\bar{\mathbf{F}}_0-\mathbf{F}_{\mathrm{s}} \tag{39}$$

In summary, one can use the Euler-Newton method to solve the above equations in each time step.

4. Solution of nonlinear equations

The Euler-Newton method is one of the common methods used for solving nonlinear equations. It is also called incremental iteration method, meaning that the load is applied according to the given load factor in some steps and the load incremental iteration calculated for each step. Let $\mathrm{u}_{\mathrm{m}}^{0}$ and u_{m} be the initial and final value of displacement, λ_{m} be the given load factor in step m^{th} and $\mathbf{F}$ be the total load. The iterative formula for step m^{th} is [51]

$$\mathbf{u}_{\mathrm{m}}^{0}=\mathbf{u}_{\mathrm{m-1}} \tag{40}$$

$$\mathbf{F}_{\mathrm{m}}=\lambda_{\mathrm{m}}\mathbf{F} \tag{41}$$

$$\boldsymbol{\psi}_{\mathrm{m}}^{\mathrm{i}}=\mathbf{F}_{\mathrm{m}}-\mathbf{F}_{\mathrm{s,m}}=\mathbf{F}_{\mathrm{m}}-\int_{V_0}\left(\mathbf{B}^{\mathrm{i}}\right)^{\mathrm{T}}\left(\mathbf{S}_{\mathrm{m}}+\Delta\mathbf{S}^{\mathrm{i}}\right)\mathrm{dV}_0 \tag{42}$$

$$\delta\left(\Delta\mathbf{u}_{\mathrm{m}}^{\mathrm{i}}\right)=-\left(\mathbf{K}_{\mathrm{L,m}}^{\mathrm{i}}+\mathbf{K}_{\mathrm{s,m}}^{\mathrm{i}}\right)^{-1}\boldsymbol{\psi}_{\mathrm{m}}^{\mathrm{i}} \tag{43}$$

$$\Delta\mathbf{u}_{\mathrm{m}}^{\mathrm{i+1}}=\Delta\mathbf{u}_{\mathrm{m}}^{\mathrm{i}}+\delta\left(\Delta\mathbf{u}_{\mathrm{m}}^{\mathrm{i}}\right) \tag{44}$$

where $\mathbf{F}_{\mathrm{m}}$ is the total load after the m^{th} load increment applied, $\Delta\mathbf{F}_{\mathrm{m}}=\left(\lambda_{\mathrm{m}}-\lambda_{\mathrm{m-1}}\right)\mathbf{F}=\Delta\lambda_{\mathrm{m}}\mathbf{F}$ is the m^{th} load increment, $\mathbf{F}_{\mathrm{s,m}}^{\mathrm{i}}$ is the nodal force after the i^{th} iteration of the m^{th} load increment, $\boldsymbol{\psi}_{\mathrm{m}}^{\mathrm{i}}$ is the unbalanced force, $\delta\left(\Delta\mathbf{u}_{\mathrm{m}}^{\mathrm{i}}\right)$ is the displacement increment after the i^{th} iteration of the m^{th} load increment.

We will continue to iterate until $\left\|\boldsymbol{\psi}\left(\boldsymbol{\delta}^{\mathrm{i}}\right)\right\|\le\alpha_{\mathrm{q}}\left\|\mathbf{R}\right\|$ with α_{q} being a predetermined tolerance, and when the convergence criterion is satisfied, one takes $\mathbf{u}_{\mathrm{exact}}\approx\mathbf{u}_{\mathrm{m}}$.

Additionally, some key steps of solution procedure for the implementation of the present work can be summarized as follows:

1. Pre-processing of the geometric model and define relevant parameters
2. The Bézier extraction operator
3. Assemble the global load array
4. Loop over all load steps
   a. Ascertain the elato-plastic modulus and assemble the global stiffness matrix including both linear and nonlinear parts
   b. Use the Euler-Newton method for solving the linearized balance equation
   c. Calculate the stress and strain increment at each iteration step
   d. Calculate the total displacement and stress of the load step
5. Post-processing of the calculation results

5. Numerical examples and discussions

The merits of the present method for 3D elasto-plastic large deformation analysis described in the previous sections are illustrated here through numerical examples, showing the accuracy of computed numerical results. To this end, three representative numerical examples such as a block with a cylinder hole under tension, a partially loaded elasto-plastic block, and a local compression bending cylinder are considered.

In three numerical examples, the distribution of displacements and von Mises stress, the force-displacement curves, and plastic zone are all presented, investigated and discussed, addressing the accuracy and effectiveness of our developed IGA based on Bézier extraction of NURBS. To verify the accuracy of our developed approach, all the numerical examples have additionally been computed the same using 3-D FEM via ABAQUS, since proper reference solutions are not available in literature. In particular, the second-order elements in IGA based on Bézier extraction and second-order elements (20-node hexahedron elements) in FEM are taken.

In the numerical examples, unless stated otherwise the following material parameters are adopted: the Young's modulus $\mathrm{E}=2.1\times10^{5}\ \mathrm{MPa}$ and the Poisson ratio $\nu=0.3$, and the uniaxial initial yield stress $\sigma_{\mathrm{s}}^{0}=440\ \mathrm{MPa}$ and the hardening modulus $\mathrm{H}=0$, which implies that a perfect elasto-plastic model is employed. The von Mises yield criterion is used, while the incremental step

loading technique is applied. Here, α_q =0.001 is adopted.

5.1 A block with a cylinder hole under tension

The first numerical example of elasto-plastic large deformation problems deals with a bock with a cylinder hole under tension whose geometry is schematically depicted in Fig. 3a. The radius of the hole is 5m, while the length, width and height of the block are set to be 36m, 20m and 10m, respectively. In this example, the maximum acting load is set by p=225 MPa. Only a quarter of block as depicted in Fig. 3b is modeled, which is to reduce the computational time, due to the double symmetry of the geometry. As mentioned already, the reference solutions for this example are conducted by FEM (ABAQUS).

Figure 4 shows a physical mesh of 10×5×5 elements (or 1764 DOFs) used for the IGA simulation based on Bézier extraction of NURBS, and a mesh of 4335 Q20 elements (or 60072 DOFs) of the FEM analysis. In this example, we concentrate our investigation on the accurate comparison of the distributions of displacements and von Mises stress between our developed IGA and the FEM, see Figs. 5-7. As observed from the figures, a good agreement between two solutions is obtained. While the FEM, as usual, takes a higher number of elements or DOFs to be able to achieve the acceptable results, our developed method, in contrast, offers good results with less effort. This in general is known as major advantages of employing the IGA.

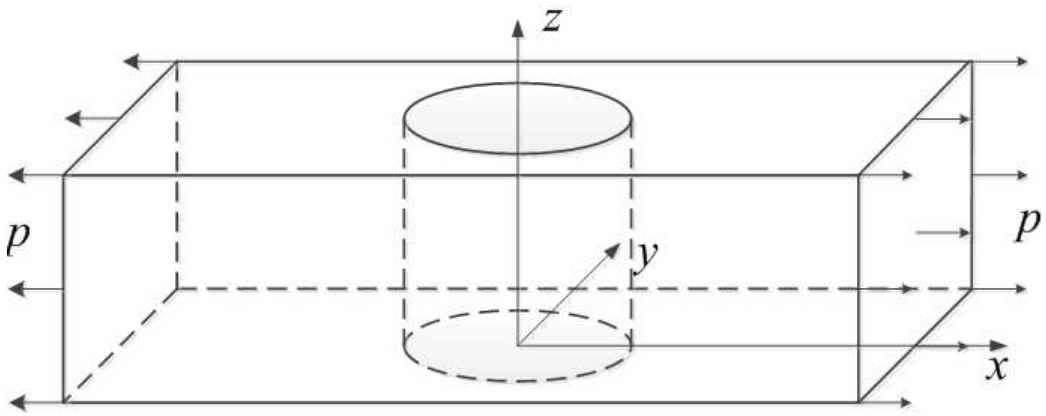

(a)

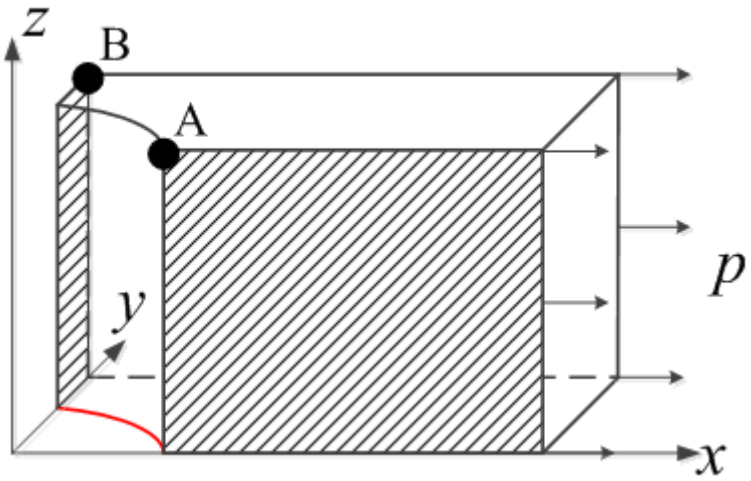

(b)

Fig. 3 Schematic representation of a block with a cylinder hole (a), and its quarter model (b), the normal displacements on the shadow planes of the quarter model are constrained. Two typical points with their coordinates such as A(5m,0,10m) and B(0,10m,10m) are considered to estimate the appropriate numerical results.

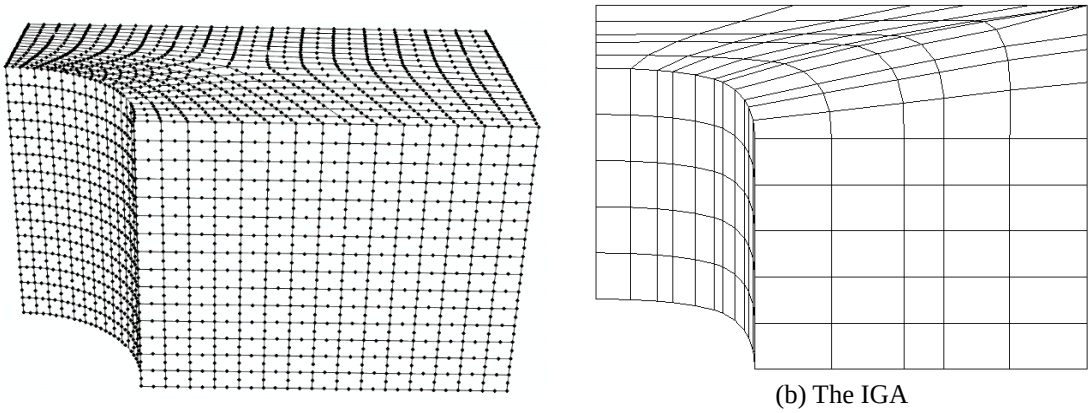

(a) The FEM (ABAQUS)

(b) The IGA

Fig. 4 Mesh discretization of the quarter of the block using the FEM (a) and the IGA (b)

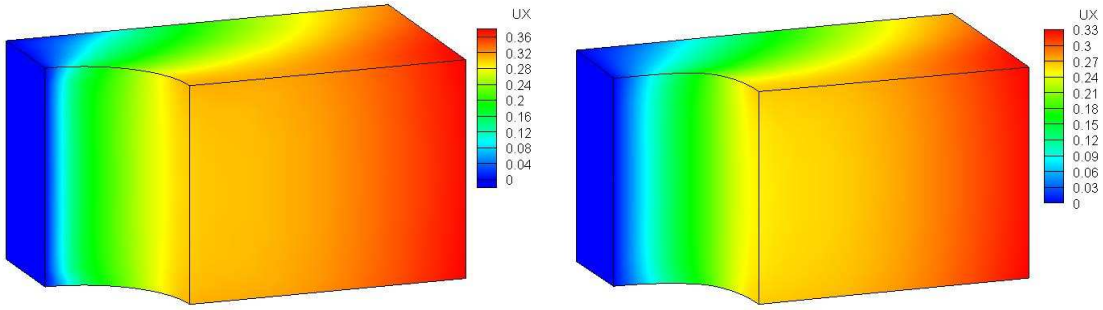

(a) The FEM (4335 elements, 60072 DOFs)

(b) The IGA (250 elements, 1764 DOFs)

Fig. 5 Comparison of the displacement u_x for the quarter of a block for $p = 225MPa$ (unit:m)

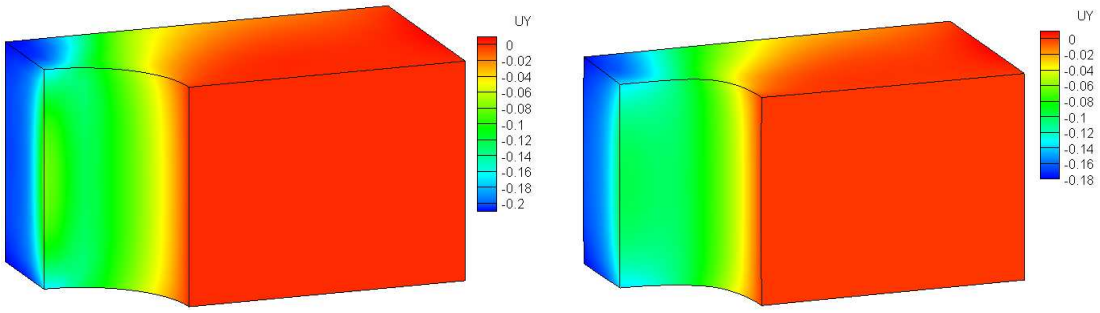

(a) The FEM(4335 elements, 60072 DOFs)

(b) The IGA (250 elements, 1764 DOFs)

Fig. 6 Comparison of the displacement u_y for the quarter of a block for $p = 225MPa$ (unit:m)

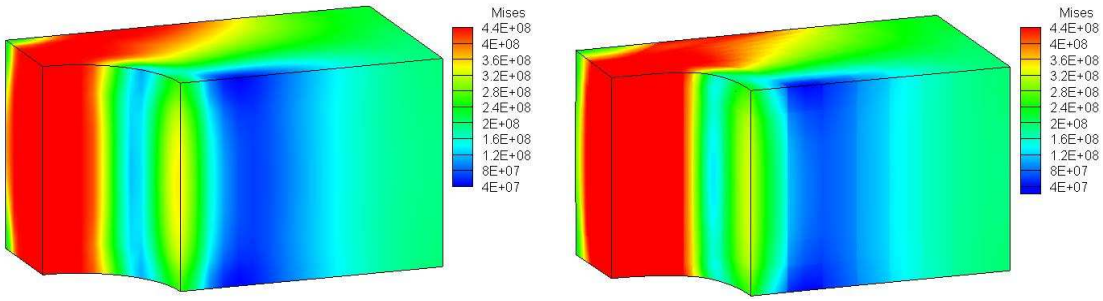

(a) The FEM (4335 elements, 60072 DOFs) (b) The IGA (250 elements, 1764 DOFs)

Fig. 7 Comparison of the von Mises stress for the quarter of a block for $p = 225\text{MPa}$ (unit:Pa)

In this work, the force-displacement curve is also an important aspect to be analyzed. To this end, two typical points as indicated in Fig. 3, A(5m,0,10m) and B(0,10m,10m), are chosen to visualize such load-displacement curve results. It is observed from Fig. 3b that the displacement in y-direction at point A and that in x-direction at point B are equal to zero. Thus, Figs. 8 and 9 represent the load-displacement curve on the point A and B, respectively. The accuracy of the developed IGA can be confirmed as very good agreements between two solutions are obtained.

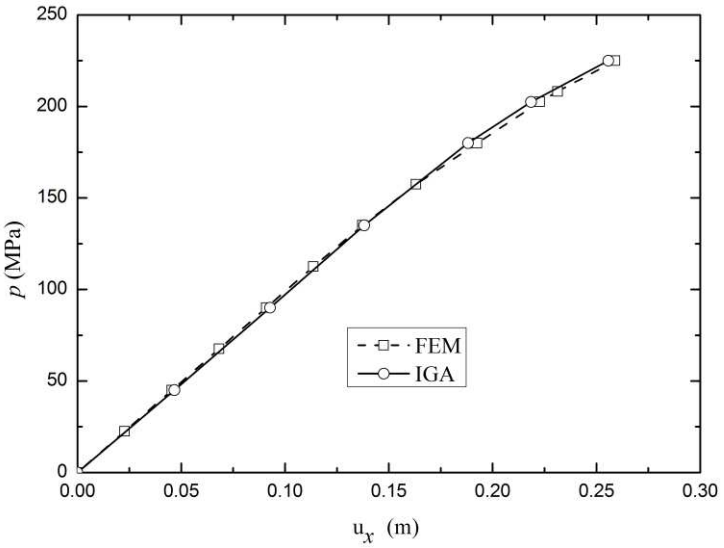

Fig. 8 Comparison of the load- x-displacement curves at point A between the developed IGA and the FEM.

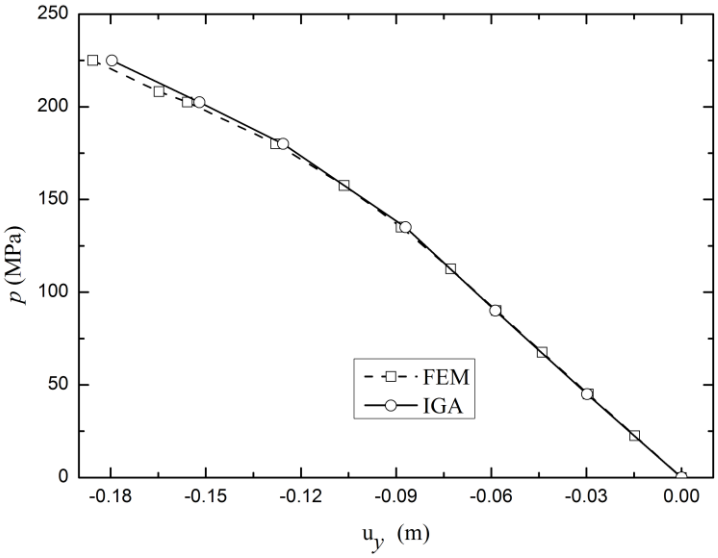

Fig. 9 Comparison of the load- y-displacement curves at point B between the developed IGA and the FEM.

Further study for mesh convergence using the proposed IGA is shown in Fig. 10, representing the variation of x-displacement along the inner bottom edge of the cylinder hole (i.e., the red curve in Fig. 3b) with different meshes. Not surprisingly, our own numerical experiment has found that adequate fine meshes can provide acceptable solutions, whereas coarse meshes, e.g., 4x2x2 elements, destroy the accuracy. For more information, we also report in Table 1 the computational time and the number of iteration during loading by the Newton-Raphson nonlinear IGA. As expected, the computational time and the number of iteration significantly increase when the meshes get finer.

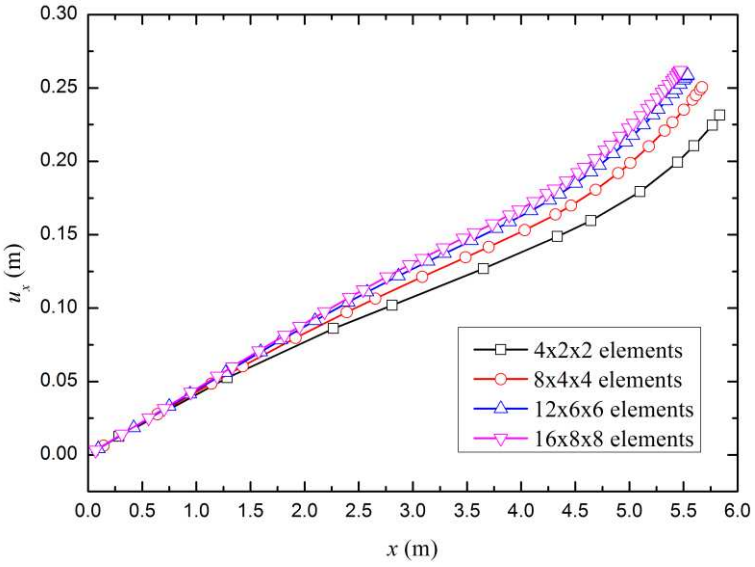

Fig. 10 The variation of x-displacement along the inner bottom edge of the cylinder hole with different meshes using the developed IGA method.

Table 1

Information of computational time and number of iteration during loading by the IGA

No. of elements	4×2×2	8×4×4	12×6×6	16×8×8
Computational time/s	58	691	2535	4027
No. of Iteration during the first loading	2	2	2	2
No. of Iteration during the second loading	9	9	9	9
No. of Iteration during the third loading	15	15	16	16
No. of Iteration during the fourth loading	32	44	48	51
No. of Iteration during the fiveth loading	76	91	98	104

Additionally, the plastic regions of the quarter of the block calculated are studied. The plastic regions calculated by our proposed IGA based on Bézier extraction compared with those derived from the FEM (ABAQUS) are thus shown in Fig. 11. It is interesting to see that the plastic zone given by the IGA is in good agreement with the plastic zone by using FEM.

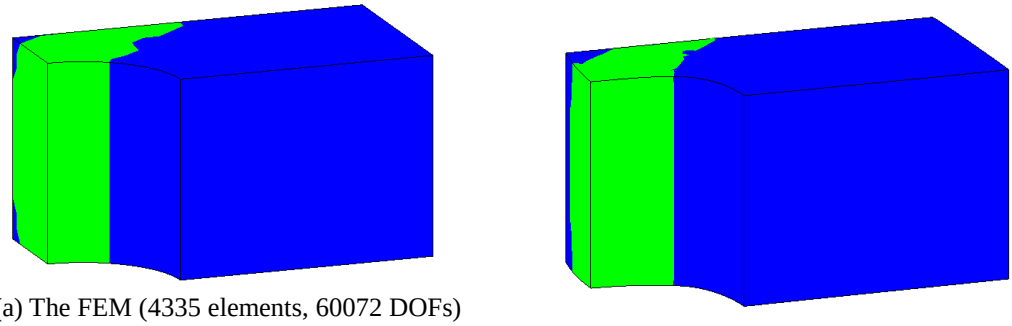

(a) The FEM (4335 elements, 60072 DOFs)

(b) The IGA (250 elements, 1764 DOFs)

Fig. 11 Comparison of the plastic regions for the quarter of a block for $p = 225\text{MPa}$ between the developed IGA and the FEM.

5.2 Partially loaded elasto-plastic block

The second example is a tridimensional elasto-plastic block under partial compression as shown in Fig. 12a. The material parameters used for the analysis are $E = 6900\ \text{MPa}$ and $\nu = 0.3$, and $\sigma_s^0 = 500\ \text{MPa}$. The maximum acting load for this example is $p = 800\text{MPa}$. Due to the double symmetry, only one quarter of the block as depicted in Fig. 12b is sufficient to be modeled to save the computational time. A physical mesh of $10\times10\times10$ elements is taken for the simulation of IGA based on Bézier extraction, while a mesh of $20\times20\times20$ Q20 elements is for the FEM analysis, see

Fig. 13. Similarly, the distributions of the displacement and the von Mises stress of the quarter of the block, the force-displacement curve, and the plastic regions, computed by the FEM (ABAQUS) and the proposed IGA based on Bézier extraction are analyzed. Figs. 14-17 respectively show comparisons of the von Mises stress and three components of displacements between two approaches. Good agreements between both solutions are obtained. The load-z-displacement curve at point A(0,0,10)m plotted in Fig. 18 calculated by the IGA agrees well with the curve obtained by the FEM. The plastic regions are depicted in Fig. 19. Overall, the results of both approaches are similar, but the FEM yields the plastic zone slightly larger than the IGA.

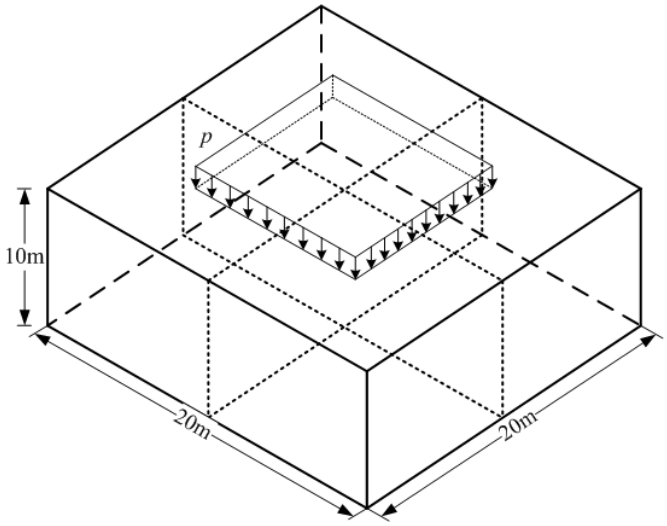

(a)

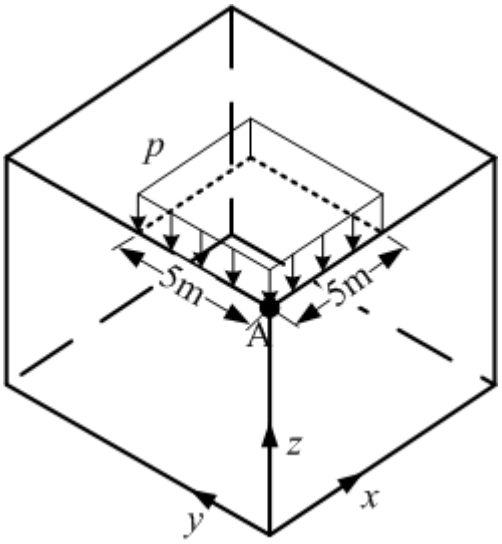

(b)

Fig. 12 Schematic representation of the full model of a block under partial compression (a), and its quarter model (b).

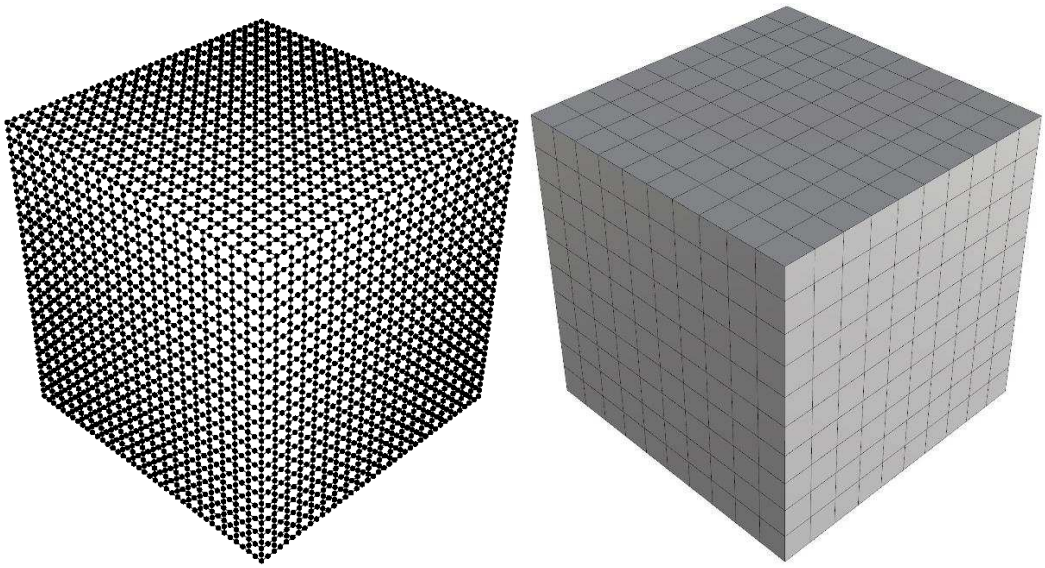

(a) FEM 20×20×20 (b) IGA 10×10×10

Fig. 13 Mesh discretization of a quarter of the block using the FEM (ABAQUS) (a) and the developed IGA (b)

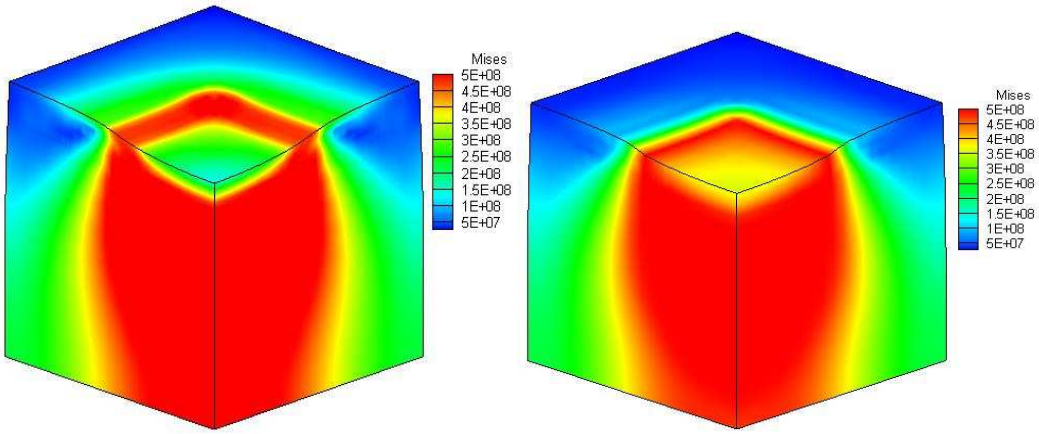

(a) The IGA (b) The FEM

Fig. 14 Comparison of the von Mises stress of a quarter of the block between the developed IGA and FEM (unit: Pa).

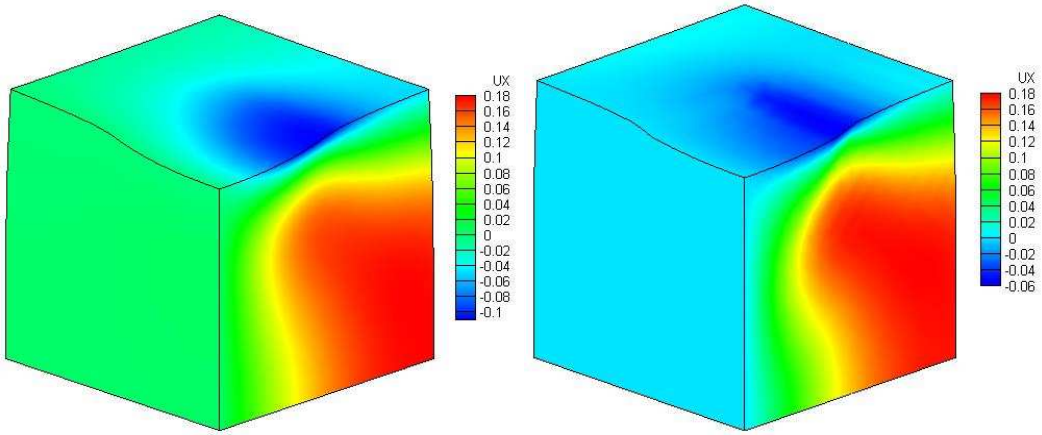

(a) The IGA (b) The FEM

Fig. 15 Comparison of the displacement u_x of a quarter of the block between the

developed IGA and FEM (unit:m)

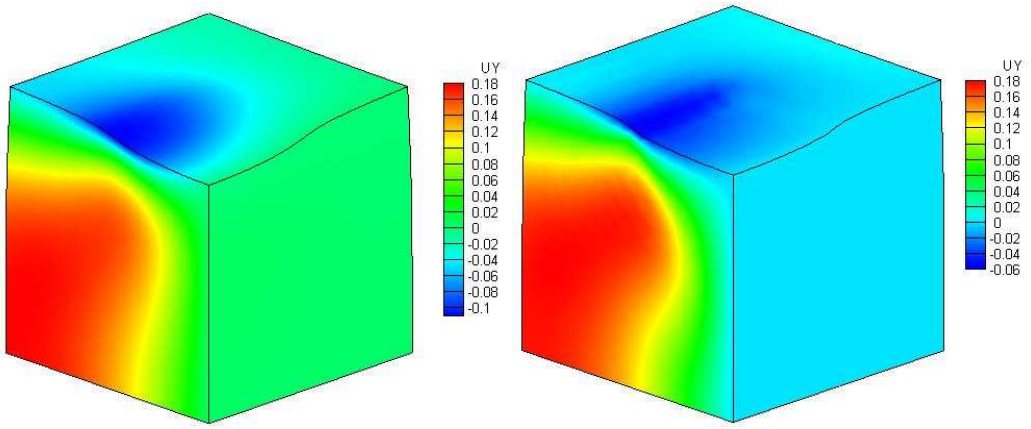

(a) The IGA (b) The FEM

Fig. 16 Comparison of the displacement u_y of a quarter of the block between the developed IGA and FEM (unit:m)

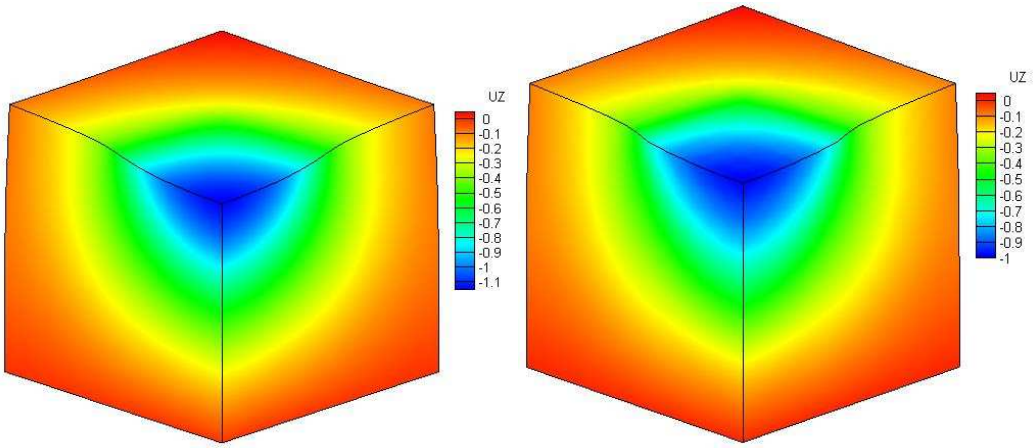

(a) The IGA (b) The FEM

Fig. 17 Comparison of the displacement u_z of a quarter of the block between the developed IGA and FEM (unit:m)

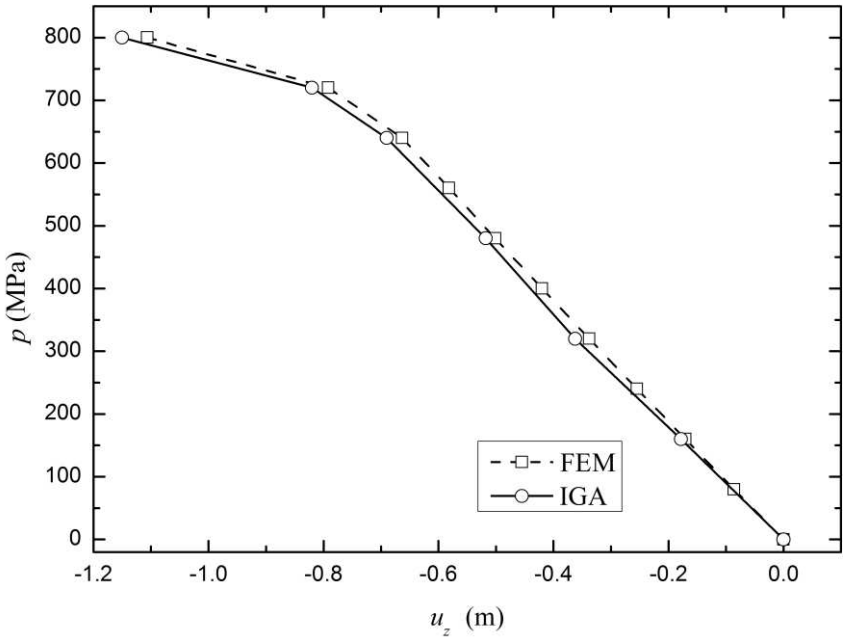

Fig. 18 Comparison of the load- z-displacement curve at point A (0,0,10)m between the developed IGA and FEM.

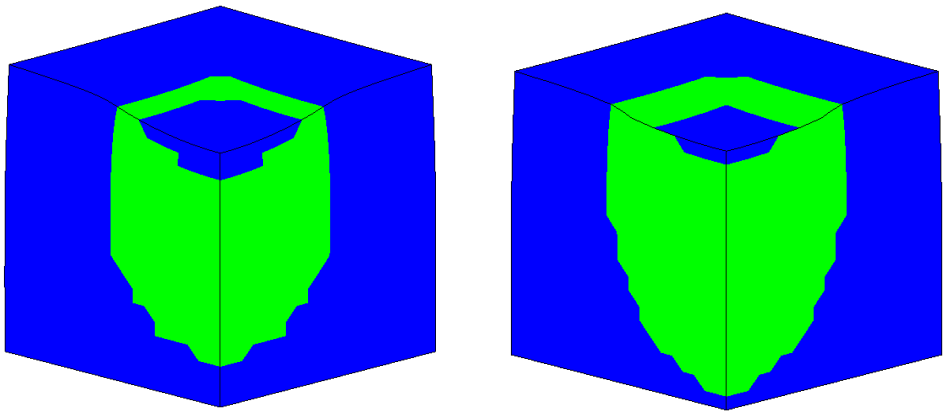

(a) The IGA (b) The FEM

Fig. 19 Comparison of the plastic zone of a quarter of the block for $p = 800\text{MPa}$ between the developed IGA and FEM.

5.3 A three-dimensional curved beam

The last numerical example deals with a more complicated configuration, a curved beam as shown in Fig. 20, in which the inner and the outer radii are set to be $a = 0.8\,\text{m}$ and $b = 1\text{m}$, and length $L = 1\,\text{m}$. The maximum acting load for this curved beam is $p = 49\text{MPa}$. For the boundary conditions: the displacements in x- and z-directions at the left face (x=0) are fixed. The displacements in y-direction at the right face (y=0) are also fixed. Typical meshes used for the FEM and IGA

simulations are shown in Fig. 21. Similar to the previous examples, the calculation results of the two methods are subsequently shown in Figs. 22-24, in which the displacements, the von Mises stress, and force-displacement curve at point A(0.8, 0,1)m, and the plastic regions obtained by the developed IGA match well with those using FEM (ABAQUS). The plastic zone of this curved beam obtained by the IGA agrees well with the FEM. It is important to note that, while our IGA always offers efficient solutions with less effort as a smaller number of DOFs is used. In contrast, the FEM however requires much larger DOFs.

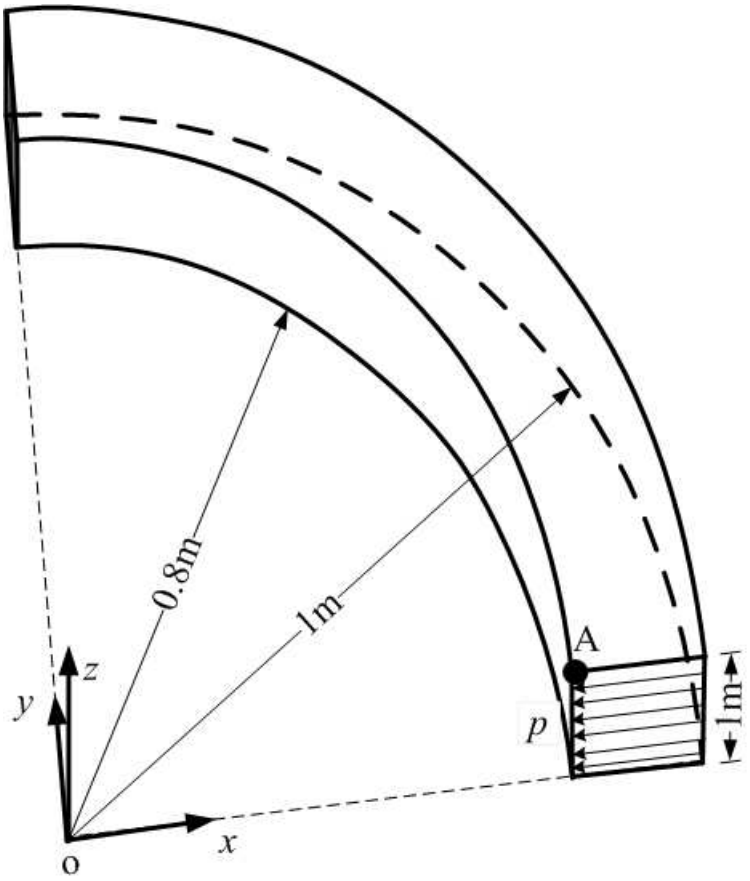

Fig. 20 Schematic representation of a three-dimensional curved beam.

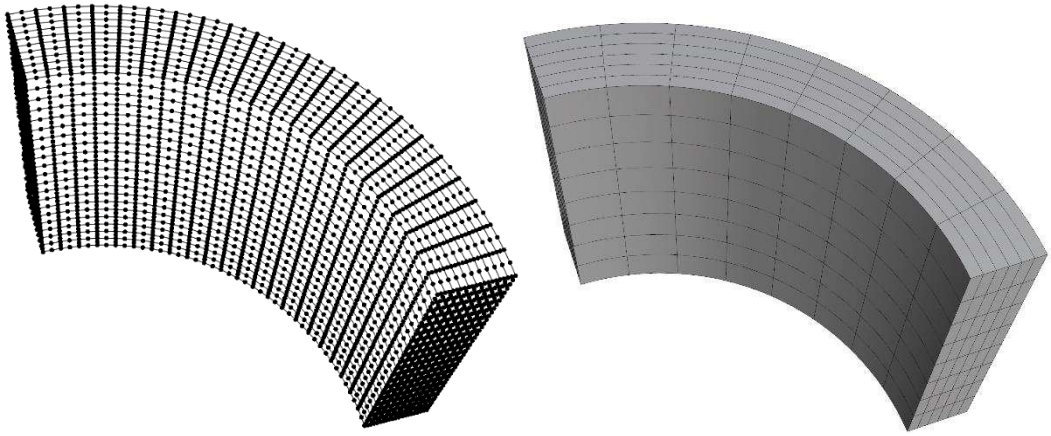

(a) FEM 20×10×20 (b)IGA 8×6×8

Fig. 21 Mesh discretization of the curved beam by the FEM (a) and the IGA (b)

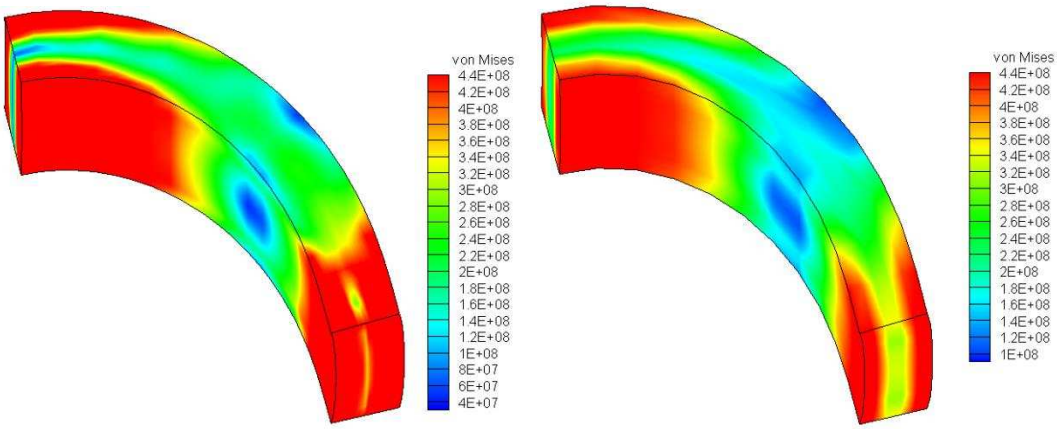

(a) The IGA (b) The FEM

Fig. 22 Comparison of the von Mises stress of the curved beam between the developed IGA and FEM

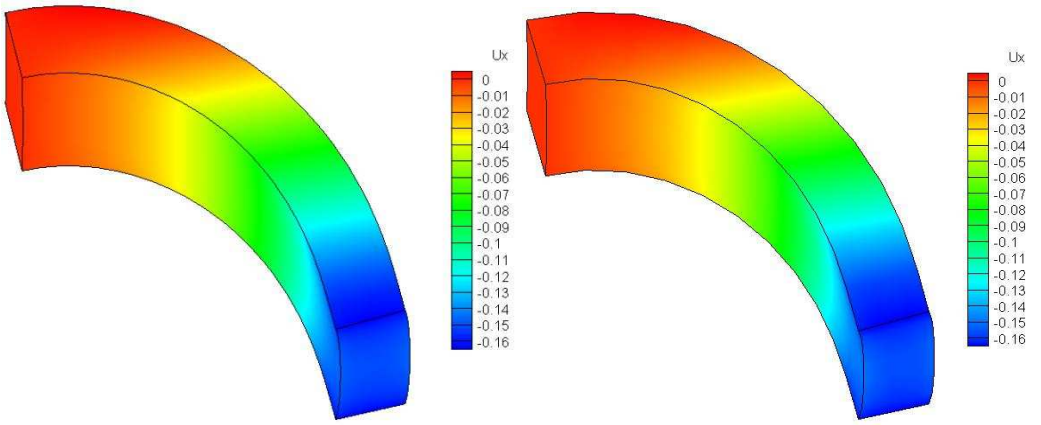

(a) The IGA (b) The FEM

Fig. 23 Comparison of the displacement u_x of the curved beam between the developed IGA and FEM.

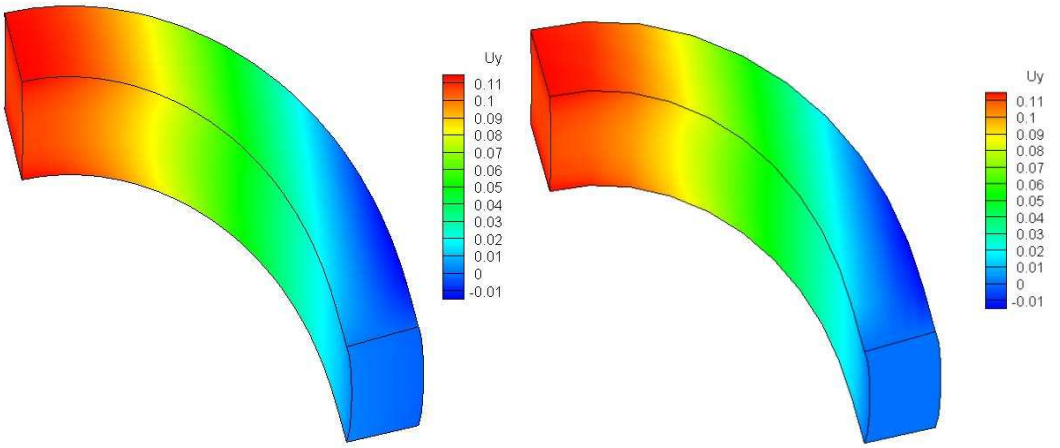

(a) The IGA (b) The FEM

Fig. 24 Comparison of the displacement u_y of the curved beam between the

developed IGA and FEM.

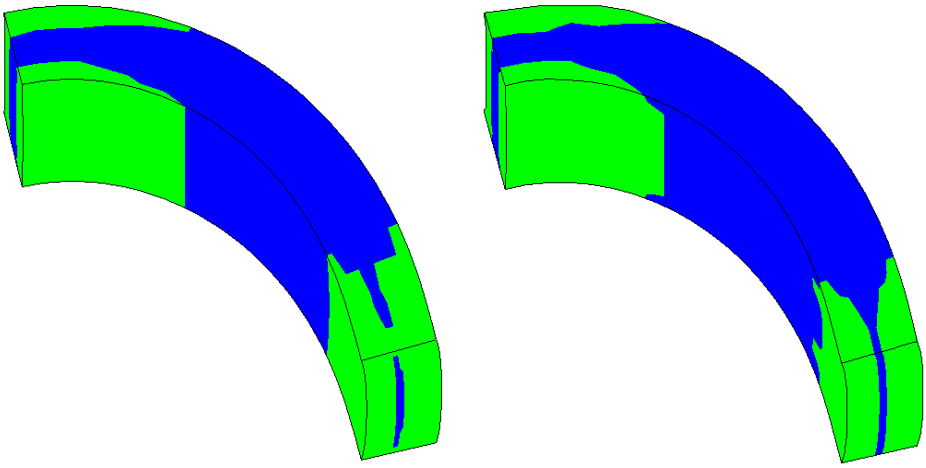

(a) The IGA (b) The FEM

Fig. 25 Comparison of the yielded regions of the curved beam between the developed IGA and FEM.

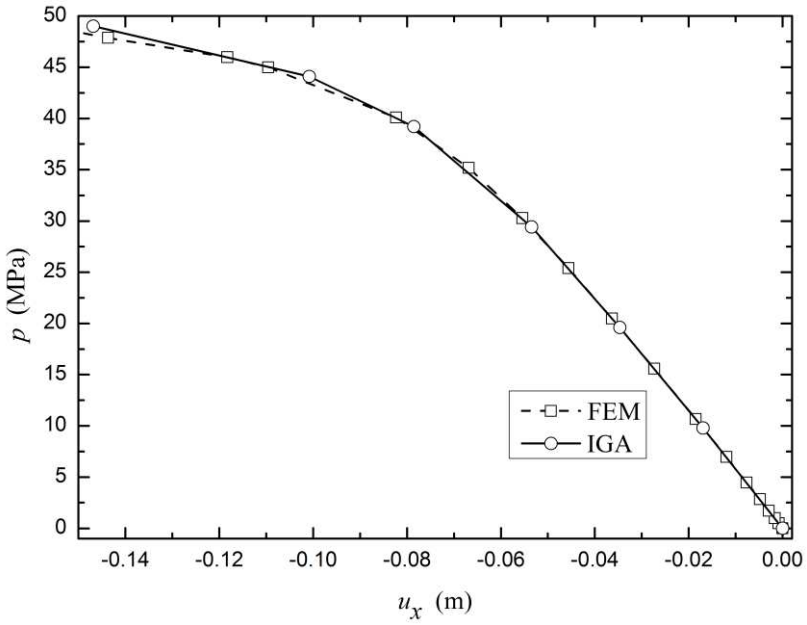

Fig. 26 Comparison of the load- x-displacement curve at the point A(0.8,0,1)m between the developed IGA and FEM.

6. Conclusions

In this paper, we have extended the IGA based on Bézier extraction of NURBS to the simulation of elasto-plastic large deformation problems in three-dimension (3-D), demonstrating the accuracy and effectiveness of the present method. All numerical examples of the elasto-plastic large deformation problems have additionally been computed using FEM based on ABAQUS, and their computed results

have been used as reference solutions for validation of the accuracy of the present IGA. The displacements, distributions of von Mises stress, convergence, plastic yielded region, and the force-displacement curves computed by the IGA are investigated and compared. In all cases, good agreements between two solutions are found. It is indicated from the obtained results that the IGA based on Bézier extraction of NURBS can effectively be used to solve the problems of elasto-plastic large deformation in 3-D, by which less elements than the FEM but can yield acceptable accuracy. More importantly, among many desirable features of the IGA, and the distortion issue of the meshes encountered when modeling elasto-plastic large deformation problems often needs a special treatment from the traditional FEM approaches, which however is not the case in terms of the IGA.

Acknowledgements

This work was supported by the National Sci-Tech Support Plan of China (Grant No. 2015BAB07B10). The financial support is gratefully acknowledged.

References

[1] MC Oliveira, JL Alves, BM Chaparro, LF Menezes. Study on the influence of work-hardening modeling in springback prediction. International Journal of Plasticity 2007; 23:516-543.

[2] AR Khoer, RW Lewis. Adaptive finite element remeshing in a large deformation analysis of metal powder forming. Int. J. Numer. Meth. Eng. 1999; 45:801-820.

[3] JP Pascon, HB Coda. Large deformation analysis of elastoplastic homogeneous materials via high order tetrahedral finite elements. Finite Elements in Analysis and Design. 2013; 76:21-38.

[4] JH Chiou, JD Lee, AG Erdman. Development of a three-dimensional finite element program for large strain elastic-plastic solids. Computers & Structures 1990; 36:631-645.

[5] J.T. Oden, Finite Elements of Nonlinear Continua. New York: McGraw-Hill, 1972

[6] T. Belytschko, WK Liu, B. Moran, K.I. Elkhodary. Nonlinear Finite Elements for Continua and Structures, 2nd Ed. UK, John Wiley & Sons, Ltd, 2014.

[7] O.C. Zienkiewicz, R.L. Taylor. The Finite Element Method. New York: McGraw-Hill, 1991.

[8] S Reese, P Wriggers, BD Reddy. A new locking-free brick element technique for large deformation problems in elasticity. Computers & Structures 2000; 75:291-304.

[9] MA Puso, J Solberg. A stabilized nodally integrated tetrahedral. Int. J. Numer. Meth. Eng. 2006; 67:841-867.

[10] P Areias, K Matous. Stabilized four-node tetrahedron with nonlocal pressure for modeling hyperelastic materials. Int. J. Numer. Meth. Eng. 2008; 76:1185-1201.

[11] A. Duster, E. Rank, A p-version finite element approach for two-and three dimensional problems of the J2 flow theory with non-linear isotropic hardening, International Journal for Numerical Methods in Engineering 53 (1) (2001) 49–63.

[12] JP Pascon, HB Coda. Analysis of elastic functionally graded materials under large displacements via high-order tetrahedral elements. Finite Elem. Ana. Des. 2012; 50:33-47.

[13] JP Pascon, HB Coda. High-order tetrahedral finite elements applied to large deformation analysis of functionally graded rubber-like materials. Appl. Math. Model. 2013; 37:8757-8775.

[14] JP Pascon, HB Coda. Large deformation analysis of functionally graded elastoplastic materials via solid tetrahedral finite elements. Computers & Structures 2015; 146:59-75.

[15] J. C. Simo, A framework for finite strain elasto-plasticity based on maximum plastic dissipation

and the multiplicative decomposition. Part I: continuum formulation, Computer Methods in Applied Mechanics and Engineering 66 (1988) 199-219.

[16] J. C. Simo, A framework for finite strain elasto-plasticity based on maximum plastic dissipation and the multiplicative decomposition. Part II: computational aspects, Computer Methods in Applied Mechanics and Engineering 68 (1988) 1-31.

[17] T.J.R. Hughes, J.A. Cottrell, Y. Bazilevs, Isogeometric analysis: CAD, finite elements, NURBS, exact geometry and mesh refinement, Computer Methods in Applied Mechanics and Engineering 194(39-41)(2005)4135-4195.

[18] S.H. Yin, J.S. Hale, T.T. Yu, T.Q. Bui, S.P.A. Bordas, Isogeometric locking-free plate element: a simple first order shear deformation theory for functionally graded plates, Composite Structures 118(2014)121-138.

[19] T.T. Yu, S.H.Yin, T.Q. Bui, S. Hirose, A simple FSDT-based isogeometric analysis for geometrically nonlinear analysis of functionally graded plates, Finite Elements in Analysis and Design 96(2015)1-10.

[20] S.H. Yin, T.T. Yu, T.Q. Bui, S.F. Xia, S. Hirose, A cutout isogeometric analysis for thin laminated composite plates using level sets, Composite Structures 127(2015)152-164.

[21] N. Valizadeh, S. Natarajan, O.A. Gonzalez-Estrada, T. Rabczuk, T.Q. Bui, S.P.A. Bordas, NURBS-based finite element analysis of functionally graded plates: static bending, vibration, buckling and flutter, Compos Struct 99(2013)309–326.

[22] G. Bhardwaj, IV. Singh, B.K. Mishra, Q.T. Bui, Numerical simulation of functionally graded cracked plates using NURBS based XIGA under different loads and boundary conditions, Compos Struct. 126 (2015) 347–359.

[23] T.T. Yu, S.H. Yin, T. Q. Bui, S.F. Xia, S. Tanaka, S. Hirose. NURBS-based isogeometric analysis of buckling and free vibration problems for laminated composites plates with complicated cutouts using a new simple FSDT theory and level set method. Thin-Walled Structures 101 (2016) 141-156.

[24] P. Kang, S.K. Youn, Isogeometric analysis of topologically complex shell structures, Finite Elements in Analysis and Design 99(2015)68-81.

[25] S.H. Yin, T.T. Yu, T.Q. Bui, M.N. Nguyen. Geometrically nonlinear analysis of functionally graded plates using isogeometric analysis. Eng Comput. 32(2015)519–558.

[26] W.A. Wall, M.A. Frenzel, C. Cyron, Isogeometric structural shape optimization, Comput Methods Appl Mech Eng 197(33-40)(2008)2976–2988.

[27] J. Lu, Isogeometric contact analysis: geometric basis and formulation of frictionless contact, Comput.Methods Appl.Mech.Eng.200(5–8) (2011) 726–741.

[28] Y. Bazilevs, V.M. Calo, J.A. Cottrell, T.J.R. Hughes, A. Reali, G. Scovazzi, Variational multiscale residual-based turbulence modeling for large eddy simulation of incompressible flows, Comput Methods Appl Mech Eng 197(1-4)(2007)173–201.

[29] Y. Bazilevs, V.M. Calo, T.J.R. Hughes, Y. Zhang, Isogeometric fluid–structure interaction: theory, algorithms, and computations, Comput Mech 43(1)(2008)3–37.

[30] C.V. Verhoosel, M.A. Scott, T.J.R. Hughes, R. de Borst, An isogeometric analysis approach to gradient damage models, Int J Numer Methods Eng; 86(1)(2011)115–134.

[31] T.Q. Bui, Extended isogeometric dynamic and static fracture analysis for cracks in piezoelectric materials using NURBS, Comput Methods Appl Mech Eng 295(2015)470-509.

[32] TQ Bui, S Hirose, Ch Zhang, T Rabczuk, CT Wu, T Saitoh, J Lei. Extended isogeometric analysis

for dynamic fracture in multiphase piezoelectric/piezomagnetic composites. Mech. Mater. 2016; 97:135-163.

[33] T.T. Yu, Y.L. Lai, S.H. Yin, Dynamic crack analysis in isotropic/orthotropic media via extended isogeometric analysis, Mathematical Problems in Engineering 2014, Article ID 725795, 11p.

[34] M.N. Nguyen, T.Q. Bui, T.T. Yu, S. Hirose, Isogeometric analysis for unsaturated flow problems, Computers and Geotechnics 62(2014)257-267.

[35] T. Elguedj, T.J.R. Hughes, Isogeometric analysis of nearly incompressible large strain plasticity, Comput Methods Appl Mech Eng 268 (2014) 388–416.

[36] T. Elguedj, Y. Bazilevs, V.M. Calo, T.J.R. Hughes, $\bar{B}$ and $\bar{F}$ projection methods for nearly incompressible linear and non-linear elasticity and plasticity using higher-order NURBS elements, Comput. Methods Appl. Mech. Engrg. 197 (2008) 2732–2762

[37] R.L. Taylor, Isogeometric analysis of nearly incompressible solids. Int. J. Numer. Meth. Engng 2011; 87:273–288.

[38] T. Elguedj, Y. Bazilevs, V.M. Calo, T.J.R. Hughes,F-bar Projection Method for Finite Deformation Elasticity and Plasticity using NURBS based Isogeometric Analysis, Int J Mater Form (2008) Suppl 1:1091 –1094.

[39] M.J. Borden, M.A. Scott, J.A. Evans, T.J.R. Hughes, Isogeometric finite element data structures based on Bézier extraction of NURBS, International Journal for Numerical Methods in Engineering 87(2011)15-47.

[40] T.N. Nguyen, Isogeometric Finite Element Analysis based on Bézier Extraction of NURBS and T-Splines, Norwegian University of Science and Technology, 2011.

[41] M.A. Scott, M.J. Borden, C.V. Verhoosel, T.W. Sederberg, T.J.R. Hughes, Isogeometric finite element data structures based on Bézier extraction of T-splines, International Journal for Numerical Methods in Engineering 88(2011)126-156.

[42] D.C. Thomas, M.A. Scott, J.A. Evans, K. Tew, E.J. Evans, Bezier projection: A unified approach for local projection and quadrature-free refinement and coarsening of NURBS and T-splines with particular application to isogeometric design and analysis, Comput. Methods Appl. Mech. Engrg. 284(2015)55-105.

[43] F. Irzal, J.J.C. Remmers, C.V. Verhoosel, R. de Borst, An isogeometric analysis Bézier interface element for mechanical and poromechanical fracture problems, International Journal for Numerical Methods in Engineering 97(2014)608-628.

[44] E.J. Evans, M.A. Scott, X. Li, D.C. Thomas, Hierarchical T-splines: Analysis-suitability, Bezier extraction, and application as an adaptive basis for isogeometric analysis, Comput. Methods Appl. Mech. Engrg. 284(2015)1-20.

[45] D. Schillinger, S.J. Hossain, T.J.R. Hughes, Reduced Bezier element quadrature rules for quadratic and cubic splines in isogeometric analysis, Comput. Meth Appl. Mech. Engrg. 277(2014)1-45.

[46] D. Rypl, B. Patzák B, Assessment of computation efficiency of numerical quadrature schemes in the isogeometric analysis, Engineering Mechanics 19(4)(2012)249-260.

[47] DJ Benson, Y Bazilevs, MC Hsu, TJR Hughes. Isogeometric shell analysis: The Reissner-Mindlin shell. Comput. Meth. Appl. Mech. Eng. 2010; 199: 276-289.

[48] S Lipton, JA Evans, Y Bazilevs, T Elguedj, TJR Hughes. Robustness of isogeometric structural discretizations under severe mesh distortion. Comput. Meth. Appl. Mech. Eng. 2010; 199:357-373.

[49] J.A. Cottrell, T.J.R. Hughes, Y. Bazilevs, Isogeometric analysis, John Wiley & Sons, 2009.

[50] J. C. Simo, T. J. R. Hughes, Computational Inelasticity, Springer-Verlag, New York, 1998.
[51] D.R.J. Owen, E. Hinton, Finite elements in plasticity: theory and practice, Pineridge Press, 1980.